GEOPHYSICS, VOL. 80, NO. 1 (JANUARY-FEBRUARY 2015); P. R57–R69, 17 FIGS.
10.1190/GEO2014-0100.1

Downloaded 01/23/16 to 138.67.128.33. Redistribution subject to SEG license or copyright; see Terms of Use at http://library.seg.org/

Wavefield tomography using reverse time migration backscattering

Esteban Díaz[1] and Paul Sava[1]

ABSTRACT

Reverse time migration backscattering contains kinematic information that can be used to constrain velocity models. The backscattering results from the correlation between forward scattered and backscattered wavefields from sharp interfaces, i.e., sediment-salt interfaces. The synchronization between these wavefields depends on the velocity of the sediment section and the correct interpretation of the sharp boundary. We have developed an optimization workflow in which the sediment velocity and the sharp boundary are updated iteratively. The presence of sharp boundaries in the model lead to high- and low-wavenumber components in the objective function gradient; the high-wavenumber components correspond to the correlation of wavefields traveling in opposite directions, whereas the low-wavenumber components correspond to the correlation of wavefields traveling in the same direction. This behavior is similar to reverse time migration in which the high-wavenumber components represent the reflectors (the signal) and the low-wavenumber components represent backscattering (noise). The opposite is true in tomography: The low wavenumber components represent changes to the velocity model, and the high-wavenumber components are noise that needs to be filtered out. We use a directional filter based on Poynting vectors during the gradient computation to preserve the smooth components of the gradient, thus spreading information away from the sharp boundary. Our tests indicated that velocity models are better constrained when we include the sharp boundaries (and the associated backscattering) in wavefield tomography.

INTRODUCTION

The two-way wave equation is the engine of reverse time migration (RTM) (Baysal et al., 1983; McMechan, 1983; Whitmore, 1983). This imaging technology is used routinely to obtain high-fidelity images of the subsurface. Despite the computing cost, the two-way operator has many advantages over other modeling approaches, such as downward continuation or Kirchhoff modeling. This technique is especially suited for complex geologic settings such as those with strong velocity gradients, sharp boundaries (e.g., salt bodies), and strong lateral variations. The reason for the success of RTM is that a wavefield reconstructed with the two-way operator can easily handle any dip, multipathing, and reflections from steep structures (Gray et al., 2001; Etgen et al., 2009).

RTM also produces low-wavenumber events in seismic images, which are usually referred to as RTM artifacts. The low-wavenumber energy is produced by the correlation of waves that propagate in the same direction, thus violating the assumptions of the conventional crosscorrelation imaging condition (Claerbout, 1971). Such events include backscattered waves, head waves, and diving waves. The backscattered events obstruct the image representing the subsurface reflectivity, and so they are usually considered noise. Numerous techniques can be used to remove RTM noise. In terms of filtering approach, we could divide such methods into two categories: preimaging filtering (Yoon et al., 2004; Fletcher et al., 2005; Liu et al., 2011) and postimaging filtering (Youn and Zhou, 2001; Guitton et al., 2007; Zhang and Sun, 2009; Kaelin and Carvajal, 2011). For detailed analysis of RTM backscattering events, the reader is referred to Díaz and Sava (2012).

Although the low-wavenumber energy is noise for imaging purposes, it can be used for velocity model building. This energy is the result of the correlation of waves traveling in the same direction, thus coinciding in space and time. This space and time coincidence only occurs when the wavefield extrapolation is accurate. Therefore, if the velocity model is correct, the RTM backscattering is strong because the wavefields are synchronized (Díaz and Sava, 2012). For reflected data, the space-time synchronization criterion also applies at the reflector position. Because both types of waves

Manuscript received by the Editor 14 March 2014; revised manuscript received 16 July 2014; published online 29 December 2014.
[1]Colorado School of Mines, Center for Wave Phenomena, Golden, Colorado, USA. E-mail: ediazpan@mines.edu; psava@mines.edu.
© 2014 Society of Exploration Geophysicists. All rights reserved.

Downloaded 01/23/16 to 138.67.128.33. Redistribution subject to SEG license or copyright; see Terms of Use at http://library.seg.org/

(reflected and backscattered) share the same kinematic behavior, we can design a joint optimization problem that improves the synchronization of all the data simultaneously, thus allowing us to refine the model and to use the RTM backscattering as a source of information instead of treating it as noise. RTM backscattering have been also used in the context of full waveform inversion (FWI) by Clément et al. (2001), Xu et al. (2012), and Ma and Hale (2013). They use various approaches to preserve the smooth components coming from the backscattering kernel to update the background velocity model.

To optimize the velocity model, one can choose a method that is consistent with the modeling operator (two-way). Such an inverse problem could be formulated by finding a model that produces data that resemble the observed data, as is done in FWI (Tarantola, 1984; Pratt, 1999). This data-domain approach relies on the kinematic and dynamic consistencies between the modeled and observed data. Therefore, if the propagation engine used is not dynamically consistent with the data, i.e., the modeled amplitudes are not accurate, then the chances for convergence diminish. Alternatively, one can optimize the model in the image space using techniques from the family usually referred to as wavefield tomography (Woodward, 1992; Sava and Biondi, 2004; Fliedner and Bevc, 2008; Shen and Symes, 2008; Yang and Sava, 2011a). The image-domain approach seeks the kinematic synchronization of the wavefields at an image location. Therefore, the aim of this method is to improve the image focusing rather than to match the dynamic information of the wavefields as is done in the data-domain approach. This increases the robustness of the method, but decreases its ability to construct high-resolution models.

One way to formulate the problem in the image space is by using extended images (Rickett and Sava, 2002; Sava and Fomel, 2006; Sava and Vasconcelos, 2011), from which we can extract wavefield similarities in space and time (Shen et al., 2003; Yang and Sava, 2010; Weibull and Arntsen, 2013). Extended images are normally used for optimizing the reflected data information, but Díaz and Sava (2012) show that similar to reflected data, the RTM backscattered energy also maps to zero time-lag and space-lag when the velocity model is correct.

In this paper, we demonstrate that it is possible to use the backscattered waves for image-domain wavefield tomography. Using the two-way wave equation operator allows simultaneous inversion based on the reflected and backscattered waves. We formulate the tomography problem using the adjoint state method (ASM), which is an efficient technique for gradient-based optimization (Plessix, 2006). However, the gradient computed using the ASM suffers from crosstalk between forward and backscattered waves, which produces undesirable reflector-like events. To avoid the unwanted correlations, we apply a directional filter designed to keep the contributions between wavefields traveling in the same direction during the correlation step of the gradient computation. This filter is based on the Poynting vectors of the extrapolated wavefields (Yoon et al., 2004), although other filtering techniques can be used instead.

We start this paper with a brief review of RTM backscattering kinematic properties and mapping patterns in extended images, and then we review wavefield tomography using extended images. We show how this methodology can be adapted to backscattering energy and define an objective function (OF) and its gradient, which are essential for inversion. We then illustrate how we can make use of the backscattering information for wavefield tomography, and we demonstrate our method using a complex synthetic based on the Sigsbee model (Paffenholz et al., 2002).

RTM BACKSCATTERING REVISITED

RTM backscattering is produced in the presence of sharp models, e.g., sediment-salt interfaces. In such cases, wavefields extrapolated with a two-way operator (e.g., the scalar wave equation),

$$\frac{1}{v(\mathbf{x})^2}\frac{\partial^2 u_s(\mathbf{x},t)}{\partial t^2} - \nabla^2 u_s(\mathbf{x},t) = f(\mathbf{x},t), \tag{1}$$

contain forward scattered and backscattered components. Here, $u(\mathbf{x},t)$ is the reconstructed wavefield, $v(\mathbf{x})$ is the medium velocity, and $f(\mathbf{x},t)$ is the source function. Therefore, we can write the source wavefield as a superposition of two components:

$$u_s(\mathbf{x},t) = u_s^b(\mathbf{x},t) + u_s^f(\mathbf{x},t), \tag{2}$$

where the superscripts b and f correspond to the backscattered and forward scattered wavefields from the sharp boundary, respectively.

The receiver wavefield $u_r(\mathbf{x},t)$ is solved backward in time using the recorded data $d(\mathbf{x},t)$ as the source:

$$\frac{1}{v(\mathbf{x})^2}\frac{\partial^2 u_r(\mathbf{x},t)}{\partial t^2} - \nabla^2 u_r(\mathbf{x},t) = d(\mathbf{x},t). \tag{3}$$

We can also decompose the receiver wavefield using an equivalent naming convention:

$$u_r(\mathbf{x},t) = u_r^b(\mathbf{x},t) + u_r^f(\mathbf{x},t). \tag{4}$$

Conventional imaging condition

The source and receiver wavefields allow one to construct an image with the conventional imaging condition (Claerbout, 1971) defined as the zero-lag correlation between source and receiver wavefields:

$$R(\mathbf{x}) = \sum_e \sum_t u_s(e,\mathbf{x},t) u_r(e,\mathbf{x},t). \tag{5}$$

Here, e refers to the experiment index, e.g., the shot number or plane-wave take-off angle.

If the wavefields used in imaging contain backscattering, we can substitute equations 2 and 4 into equation 5 and obtain an image that is a superposition of four individual images:

$$R(\mathbf{x}) = R^{ff}(\mathbf{x}) + R^{bb}(\mathbf{x}) + R^{bf}(\mathbf{x}) + R^{fb}(\mathbf{x}). \tag{6}$$

Following the convention in Díaz and Sava (2012), the first superscript corresponds to the source wavefield and the second to the receiver wavefield. In this total image, two components (ff and bb) provide an estimate of the reflectivity, and the other two components (fb and bf) represent backscattering. This means that the backscattering is produced from the correlation of wavefields traveling in the same direction. For example, $R^{bf}(\mathbf{x})$ is produced when the backscattered source wavefield $u_s^b(\mathbf{x},t)$ resembles the forward

Downloaded 01/23/16 to 138.67.128.33. Redistribution subject to SEG license or copyright; see Terms of Use at http://library.seg.org/

scattered receiver wavefield $u_r^f(\mathbf{x},t)$, and $R^{fb}(\mathbf{x})$ is produced with the opposite combination of the propagating wavefields. Several authors (Yoon et al., 2004; Fei et al., 2010; Liu et al., 2011) use this wavefield directionality notion to keep only the components related to reflectivity in the image and to remove everything else. Here, we use the directionality concept to keep the components that travel in the same direction during tomography.

Extended imaging condition

A generalized version of equation 5 can be used to understand the (kinematic) similarities between source and receiver wavefields. This concept is known as extended imaging (Rickett and Sava, 2002; Sava and Fomel, 2006; Sava and Vasconcelos, 2011). A general case of an extended image is defined as follows:

$$R(\mathbf{x},\boldsymbol{\lambda},\tau)=\sum_e\sum_t u_s(e,\mathbf{x}-\boldsymbol{\lambda},t-\tau)u_r(e,\mathbf{x}+\boldsymbol{\lambda},t+\tau), \tag{7}$$

where $\boldsymbol{\lambda}$ and τ are the space and time extensions of the crosscorrelation, respectively. Extended images are commonly used to produce angle gathers (Sava and Fomel, 2003, 2006; Sava and Vlad, 2011) and for velocity estimation (Shen and Symes, 2008; Yang and Sava, 2011b; Yang et al., 2013).

In the presence of sharp models, we can substitute equations 2 and 4 into equation 7. By doing so, we can differentiate between the different components of the extended image, which is similar to what we do for conventional images:

$$R(\mathbf{x},\boldsymbol{\lambda},\tau)=R^{ff}(\mathbf{x},\boldsymbol{\lambda},\tau)+R^{bb}(\mathbf{x},\boldsymbol{\lambda},\tau)+R^{bf}(\mathbf{x},\boldsymbol{\lambda},\tau)+R^{fb}(\mathbf{x},\boldsymbol{\lambda},\tau). \tag{8}$$

The reflected data maps into the components ff and bb, whereas the backscattered energy maps into the fb and bf components.

In the conventional image, $R(\mathbf{x})$ (backscattered and reflected energy) coexist above the sharp interfaces, e.g., due to the presence of a salt body. The two components are usually separated based on the spectral content (the artifacts have a low-wavenumber content, whereas the reflectivity has a high-wavenumber content). This separation is normally done using some sort of high-pass filter, such as a Laplacian (∇^2) operator (Youn and Zhou, 2001; Zhang and Sun, 2009) or by least-squares filtering (Guitton et al., 2007). The separation is not perfect in areas with similar spectral content. In the extended image space, however, the reflected and backscattered energy have unique mapping patterns (Díaz and Sava, 2012), which can be used to effectively separate both components (Kaelin and Carvajal, 2011). Díaz and Sava (2012) show that the backscattered and reflected energy share the wavefield synchronization criterion. The spatial and temporal synchronization occurs above a sharp boundary for backscattered events, whereas the synchronization occurs at the position of the reflectors for reflected data. The synthetic model shown in Figure 1a illustrates the extended image kinematic sensitivity to model error. The data in Figure 1b show two events: the earlier one corresponding to a reflector in the density model (spike in Figure 1a), and the later one resulting from a sharp contrast in the velocity model (step function in Figure 1a). The third event in the data corresponds to an internal multiple generated between the density and velocity interfaces.

Figure 2a–2c shows time-lag gathers for three different velocities. These gathers are generated using equation 7 with $\boldsymbol{\lambda}=0$ after stacking over different experiments, i.e., shots in this case. We simulate a velocity error in the first layer and adjust the sharp boundary according to the migration velocity, e.g., a low velocity shifts the boundary upward and a high velocity shifts the boundary downward. The backscattering maps vertically in the three cases; however, it deviates from $\tau=0$ when the velocity is incorrect. The time delay error in the backscattering is the same as the one produced by the reflected energy at the sharp interface. Therefore, the backscattering provides information about the sharp interface at any place in the image above it.

Figure 3a–3c shows the equivalent space-lag gather dependency with respect to the velocity error. Similar to the time-lag gathers, the

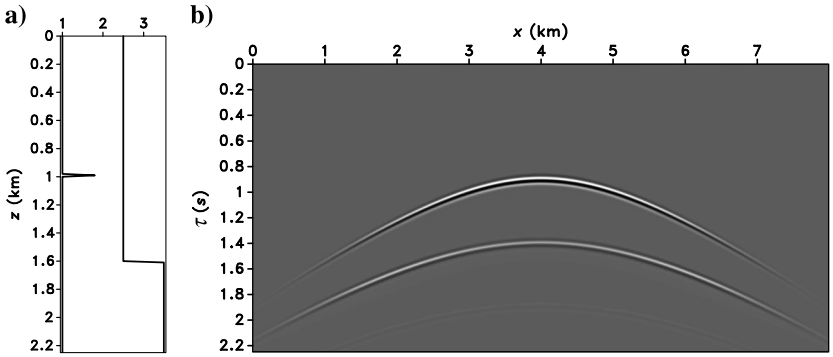


Figure 1. Synthetic experiment setup: (a) the density (spike function) model (g/cm^2) and the velocity (step function) model (km/s) and (b) the modeled data.

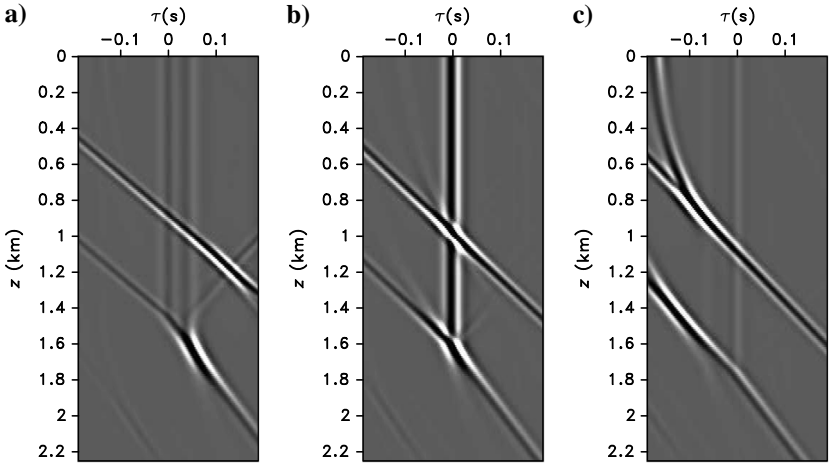


Figure 2. Time-lag gathers for (a) low, (b) correct, and (c) high velocities.

Downloaded 01/23/16 to 138.67.128.33. Redistribution subject to SEG license or copyright; see Terms of Use at http://library.seg.org/

space-lag gathers are generated after stacking the contribution from different experiments. The backscattering (mapping vertically in the gathers) spreads away from $\lambda_x = 0$ with the velocity error, thus emulating the defocusing of the reflected data. Similar to the time-lag gathers, the backscattering above the interface is the expression of the defocusing at the sharp boundary.

Because the reflected and backscattered data share similar velocity dependency, we conclude that we can design an inverse problem that optimizes both type of events simultaneously (Díaz and Sava, 2012). The following section details the velocity analysis procedure based on backscattering.

WAVEFIELD TOMOGRAPHY WITH EXTENDED IMAGES

To analyze the velocity model error, we can make use of the semblance principle, which seeks image consistency as a function of extended image parameters. Stork (1992) implements the idea using the consistency between common offset images. Symes and Carazzone (1991) exploit this concept using the differential semblance optimization (DSO) method. The DSO method can also be used to increase the flatness of angle gathers. Rickett and Sava (2002) and Sava and Fomel (2003) show that common angle gathers and extended images are related by a slant stacking operation. Therefore, these two types of common image gathers are equivalent for velocity analysis. Shen and Symes (2008) and Yang and Sava (2011a) use the consistency criterion in extended images to formulate a tomographic problem based on space-lag gathers or joint space and time-lag gathers, respectively.

Inversion with time-lag gathers

If the velocity is correct, the time-lag gathers (Sava and Fomel, 2006) show maximum focusing at zero lag. This observation derives from the fact that the source and receiver wavefields are synchronized at the reflector position. The velocity model can be improved by increasing the wavefield synchronization, which is equivalent to locating the events in the extended images as close as possible to $\tau = 0$. This can be done by minimizing the following objective function:

$$J = \frac{1}{2}\|P(\tau)R(\mathbf{x},\tau)\|^2, \tag{9}$$

where $P(\tau) = |\tau|$ is an operator that penalizes the energy outside $\tau = 0$. Note that this OF cannot drop to zero completely because in the time-lag gathers, the wavefields correlate for all values of τ. Here, we are interested in bringing the maximum of the correlation toward $\tau = 0$. However, this OF is minimum when the velocity model is correct and most of the energy in the extended image locates at $\tau = 0$.

We compute the gradient of equation 9 using the ASM (Tarantola, 1984; Plessix, 2006). The adjoint source with respect to the source wavefield for an experiment e is

$$g_s(\mathbf{x},e) = \sum_\tau P^2(\tau)R(\mathbf{x},\tau)u_r(e,\mathbf{x},t-2\tau), \tag{10}$$

and the adjoint source with respect to the receiver wavefield is

$$g_r(\mathbf{x},e) = \sum_\tau P^2(\tau)R(\mathbf{x},\tau)u_s(e,\mathbf{x},t+2\tau). \tag{11}$$

We construct the adjoint state variables by injecting the adjoint sources at the gather positions and by extrapolating the wavefields using the adjoint modeling operators. The derivation for the adjoint-state formulation is shown in Appendix A. The adjoint source wavefield $a_s(e,\mathbf{x},t)$ is reconstructed backward in time, whereas the adjoint receiver wavefield $a_r(e,\mathbf{x},t)$ is reconstructed forward in time. Using the state and adjoint state variables, the gradient with respect to the velocity model is

$$\nabla J(\mathbf{x}) = \frac{-2}{v^3(\mathbf{x})}\sum_e\sum_t \frac{\partial^2 u_s}{\partial t^2}(e,\mathbf{x},t)a_s(e,\mathbf{x},t) + \frac{\partial^2 u_r}{\partial t^2}(e,\mathbf{x},t)a_r(e,\mathbf{x},t), \tag{12}$$

where $(-2/v^3(\mathbf{x}))(\partial^2/\partial t^2)$ corresponds to the derivative of the modeling operator (equation 3) with respect to the velocity model.

In the gradient expression (equation 12), we expect to correlate state and adjoint state wavefields traveling in the same direction, which implies that the gradient is smoother than other tomography methods, such as FWI, in which the state and adjoint-state wavefields can correlate along the same direction (for diving waves and wide-angle reflections) or in the opposite direction (for reflected data with narrow angles). The relation between the scattering angle and wavenumber components for FWI is discussed in detail by Sirgue and Pratt (2004).

If backscattering is present in the wavefield, we obtain crosstalk producing reflectors in the gradients. The crosstalk in this case is generated by the correlation of wavefields traveling in the opposite direction. To attenuate the crosstalk, we can use a filter that preserves the components of wavefields traveling in the same direction and eliminates the wavefields traveling in opposite directions. We can find the direction of propagation using the approach of Yoon et al. (2004), which constructs the Poynting vectors $\mathbf{P}(e,\mathbf{x},t)$ using the equation,

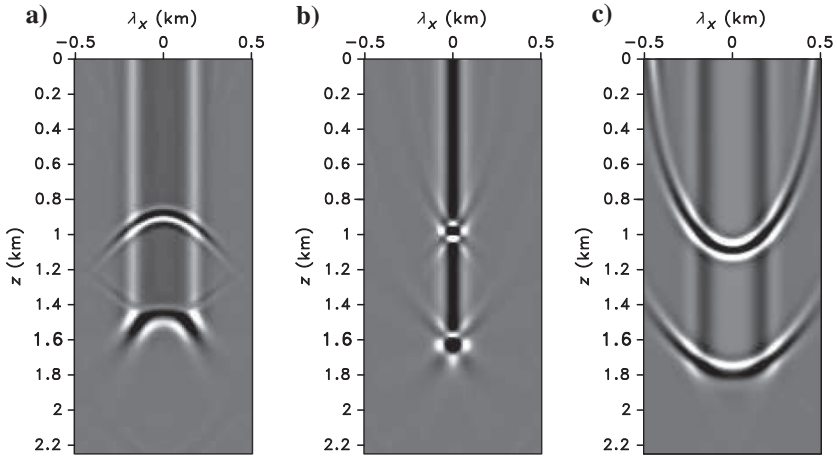


Figure 3. Space-lag gathers for (a) low, (b) correct, and (c) high velocities.

$$\mathbf{P}(e,\mathbf{x},t) \propto \frac{\partial u(e,\mathbf{x},t)}{\partial t}\nabla u(e,\mathbf{x},t), \tag{13}$$

where u can be either the source or the receiver wavefield. In practice, we use the time-averaged Poynting vectors using a Gaussian smoothing over a small time window determined by the dominant period of the data:

$$\langle \mathbf{P}(e,\mathbf{x},t)\rangle_t = \mathbf{P}(e,\mathbf{x},t) * G(t). \tag{14}$$

Here, the symbol $*$ denotes convolution and $G(t)$ is the Gaussian smoothing filter. The smoothed Poynting vector contains the propagation information of the most energetic arrival in the wavefields, which mishandle cases such as multipathing.

To keep just the wavefields components traveling in the same direction, we can compute a weighting function $W(\theta)$ with

$$\theta(\mathbf{x},t) = \cos^{-1}\left(\frac{\mathbf{P}_s(\mathbf{x},t)\cdot\mathbf{P}_r(\mathbf{x},t)}{|\mathbf{P}_s(\mathbf{x},t)||\mathbf{P}_r(\mathbf{x},t)|}\right), \tag{15}$$

such that we preserve the wavefield crosscorrelation for which $\mathbf{P}_s(\mathbf{x},t)\cdot\mathbf{P}_r(\mathbf{x},t) \approx 1$, i.e., when the direction of propagation is similar within a given tolerance. The weighting function can be designed using a cutoff angle, from which the function tapers off smoothly using a Gaussian function with standard deviation σ, which defines the range from which the angles are accepted:

$$W(\theta,a,\sigma) = \begin{cases} 1 & \text{if } 0^\circ \le \theta < a, \\ e^{-(\theta-a)^2/(2\sigma^2)} & \text{if } a \le \theta \le 180^\circ. \end{cases} \tag{16}$$

Based on this filter, we change equation 12 to

$$\nabla J(\mathbf{x}) = \frac{-2}{v^3(\mathbf{x})}\sum_e\sum_t W(\theta)\frac{\partial^2 u_s}{\partial t^2}(e,\mathbf{x},t)a_s(e,\mathbf{x},t) + W(\theta)\frac{\partial^2 u_r}{\partial t^2}(e,\mathbf{x},t)a_r(e,\mathbf{x},t). \tag{17}$$

This new gradient avoids crosstalk and emphasizes wavefields traveling in the same direction. This method increases the cost of the correlation step. If the smoothing stencil along the time axis is short, then efficient options such as checkpoint access could be used for propagating wavefields and computing the propagation directions (Symes, 2007).

Figure 4a, 4c, and 4e shows the gradient constructed using equation 12 for low, correct, and high velocities, respectively. This gradient is generated for one shot, so it is easier to appreciate the contribution of each individual seismic experiment. One can see that the intensity of the gradient with the correct velocity is lower than the obtained for either low or high velocities. One can also observe the crosstalk due to wavefields propagating in opposite directions, which appears in the gradient similar to reflectors present in a migrated image. The gradient is computed using equation 17 with a cutoff angle $a = 15^\circ$. Figure 4b, 4d, and 4f shows the crosstalk significantly attenuated.

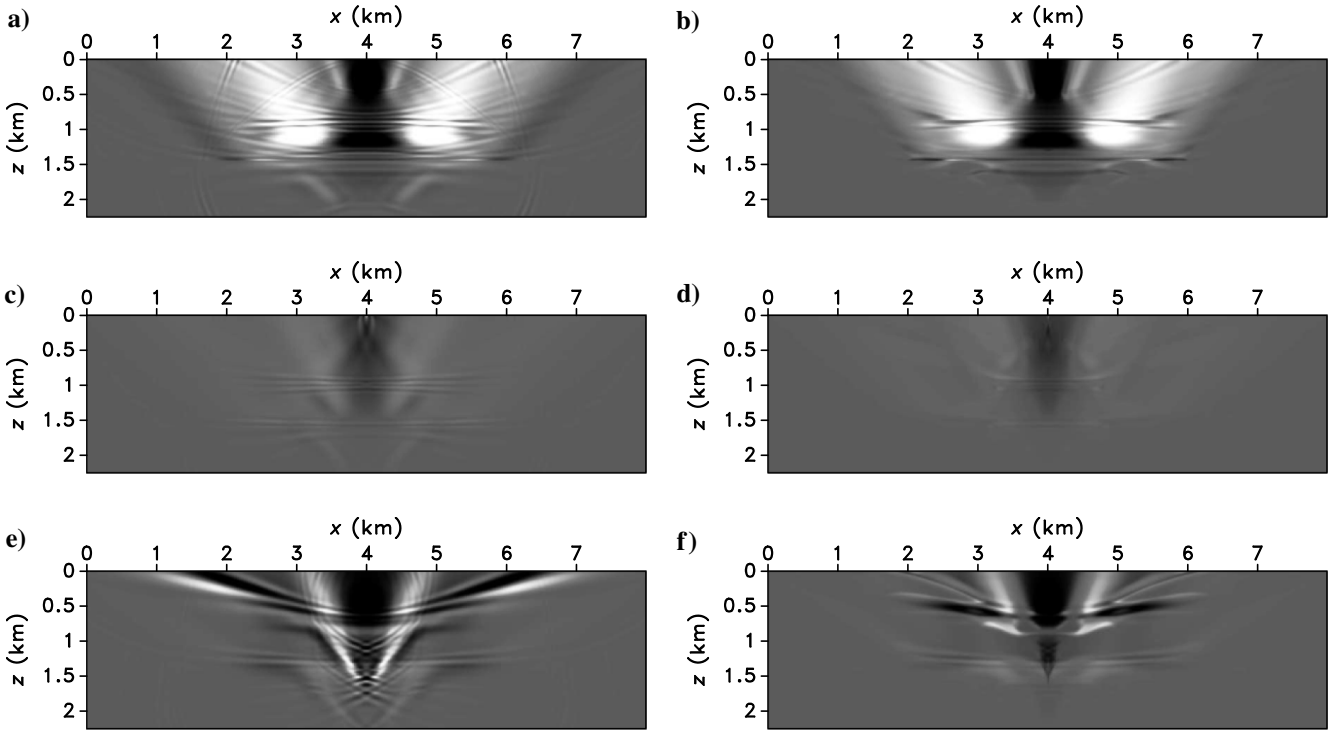


Figure 4. Gradients obtained using time-lag gathers for (a and b) low, (c and d) correct, and (e and f) high velocities. Gradients (a, c, and e) are constructed without filtering and (b, d, and f) are with filtering.

Downloaded 01/23/16 to 138.67.128.33. Redistribution subject to SEG license or copyright; see Terms of Use at http://library.seg.org/

Downloaded 01/23/16 to 138.67.128.33. Redistribution subject to SEG license or copyright; see Terms of Use at http://library.seg.org/

Inversion with space-lag gathers

We can also use the information contained in space-lag gathers (Rickett and Sava, 2002). If the velocity model is correct, then space-lag gathers focus at $(\lambda_x, \lambda_y) = (0, 0)$. If the velocity model is incorrect, the gathers contain defocused energy outside $\boldsymbol{\lambda} = 0$. This criterion is used by Shen and Symes (2008), Yang and Sava (2011a), and Weibull and Arntsen (2013) to formulate wavefield tomography using the OF

$$J = \frac{1}{2}\|P(\boldsymbol{\lambda})R(\mathbf{x}, \boldsymbol{\lambda})\|^2, \tag{18}$$

where $P(\boldsymbol{\lambda}) = |\boldsymbol{\lambda}|$ is a penalty operator. Even with correct velocity, this OF does not become zero due to the band-limited nature of the data and due to illumination effects (Yang et al., 2013). Nevertheless, this OF provides an effective criterion for velocity updating.

We compute the gradient of equation 18 using the same workflow as the one used for equation 9 (Yang and Sava, 2011a). The adjoint sources are defined as

$$g_s(\mathbf{x}, e) = \sum_{\boldsymbol{\lambda}} P^2(\boldsymbol{\lambda})R(\mathbf{x} - \boldsymbol{\lambda}, \boldsymbol{\lambda})u_r(e, \mathbf{x} + 2\boldsymbol{\lambda}, t) \tag{19}$$

for the source side and

$$g_r(\mathbf{x}, e) = \sum_{\boldsymbol{\lambda}} P^2(\boldsymbol{\lambda})R(\mathbf{x} + \boldsymbol{\lambda}, \boldsymbol{\lambda})u_s(e, \mathbf{x} + 2\boldsymbol{\lambda}, t) \tag{20}$$

for the receiver side. The only difference between the time-lag and space-lag gather formulation is in the OF and in the computation of the adjoint sources. The gradient and adjoint wavefields are computed using the same wave-equation and background velocity model as in the case of the time-lag gathers (equations 12 and 17).

Figure 5a, 5c, and 5e shows the gradients for low, correct, and high velocity, respectively. To compute these gradients, we use the space-lag gathers depicted in Figure 3a–3c, respectively. Note that for the correct velocity model Figure 5c, the gradient does not drop to zero. This is due to the band-limited nature of seismic data, which produces energy in the extended images away from zero lag even for the correct velocity model. As for the gradient constructed with the time-lag gather, one can see that the energy in the space-lag gradient is proportional to the focusing error observed in the gathers. The gradients obtained using equation 12 also contain crosstalk similar to the gradient constructed with time-lag gathers. If we apply the directional filtering during the gradient computation (equation 17), we obtain gradients with significantly lower crosstalk. Figure 5b, 5d, and 5f shows the filtered gradients for the low-, correct-, and high-velocity models, respectively.

EXAMPLES

In this section, we illustrate how to use the backscattering and reflected events with two examples: one with a simple setting including a Gaussian anomaly and the second with a truncated version of the Sigsbee model around the sediment basin. With the first example, we introduce the methodology for iterative boundary update,

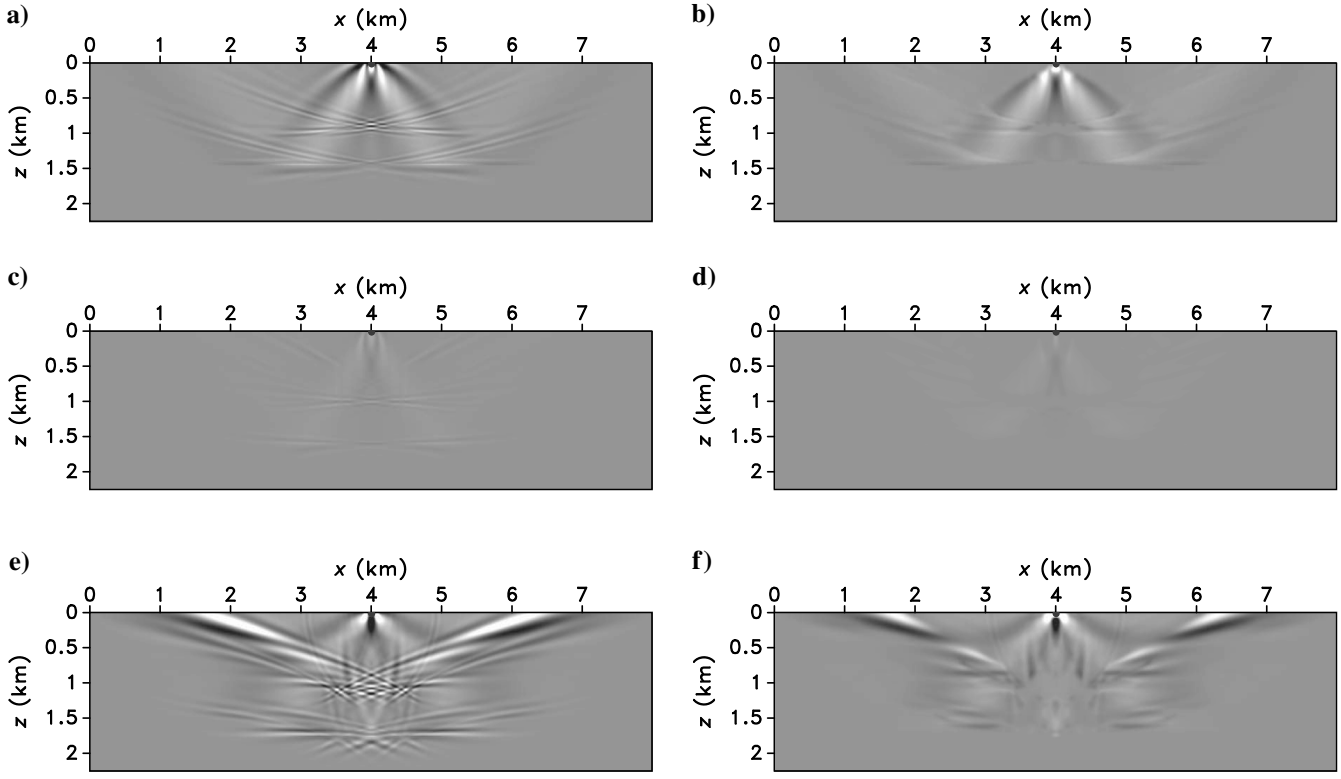


Figure 5. Gradients obtained using space-lag gathers for (a and b) low (c and d) correct, and (e and f) high velocities. Gradients (a, c, and e) are constructed without filtering and (b, d, and f) are with filtering.

Downloaded 01/23/16 to 138.67.128.33. Redistribution subject to SEG license or copyright; see Terms of Use at http://library.seg.org/

and with the second, we show its application to a more realistic example.

Simple model with a Gaussian anomaly

In this example, we test a model with a Gaussian anomaly in which we can better predict the location of the sharp boundary at each iteration. The model consists of a homogeneous background model of 2 km/s with a positive Gaussian anomaly of +15% relative to the background, shown in Figure 6a. We create data with a surface receiver array and 41 sources evenly distributed. The data contain five reflectors: The deepest reflector originates at the sharp boundary, and the others generate from discontinuities in the density model, which is only used to generate the data. Figure 7a and 7b shows the correct image and space-lag gathers for the correct model, respectively. We perform two inversion tests , the first with the conventional approach (no sharp boundary), using the starting model shown in Figure 6b and the second test using the starting model depicted in Figure 6c. Figures 8a and 9a show the images for the starting model without and with the sharp boundary, respectively. The boundary in the model is interpreted from Figure 8a.

The initial space-lag gathers are shown in Figures 8b and 9b for starting velocities without and with a sharp boundary, respectively. The gathers lag axis ranges from −0.4 to 0.4 km. Note the backscattering in Figure 9b, which highlights the defocusing of the deepest event everywhere above this event.

We perform these two inversions using a steepest descent solver with a parabolic line search. For each case, we use 10 iterations. After both inversions, the extended images have better focusing as shown in Figures 10b and 11b. Figures 10a and 11a show the

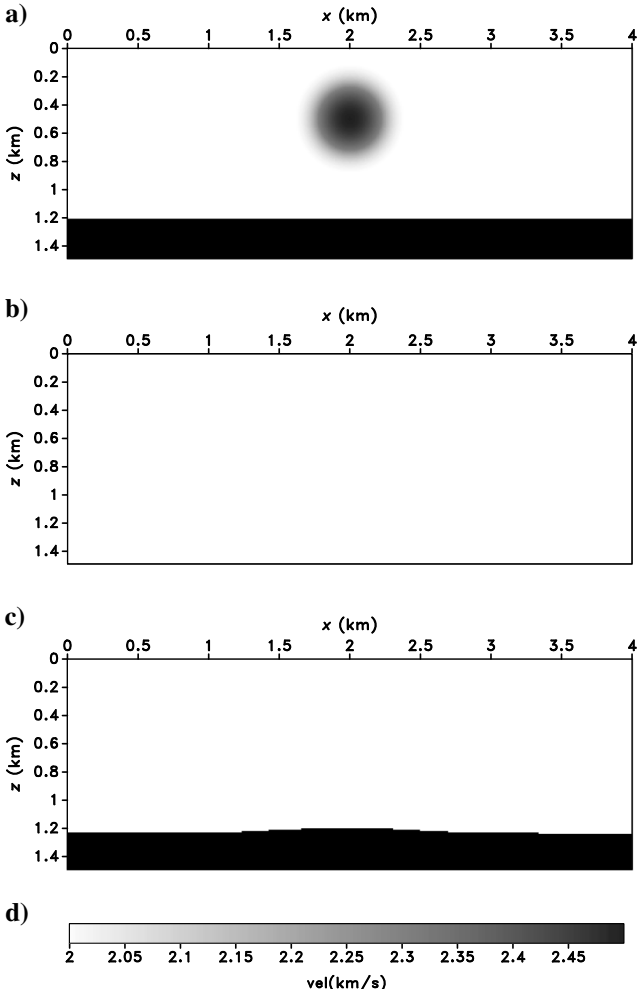


Figure 6. (a) Gaussian velocity model, (b) starting velocity without the sharp boundary, (c) starting model with the sharp boundary, and (d) the corresponding color bar.

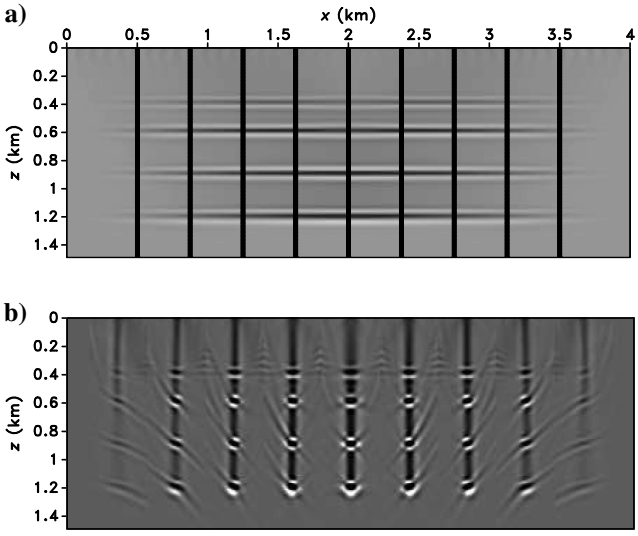


Figure 7. (a) Conventional image from the true model in Figure 6a and (b) its space-lag gathers. The blue lines show the location of the gathers.

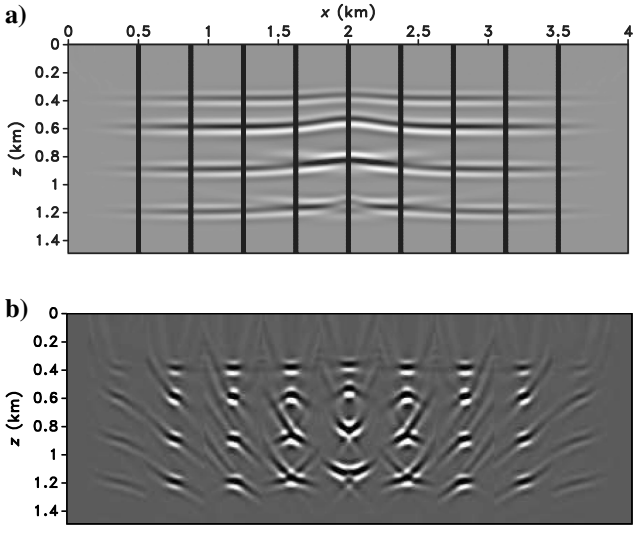


Figure 8. (a) Conventional image from the starting model in Figure 6b and (b) its space-lag gathers. Note the structural anomaly in the middle of the image (top). Compare with Figure 10a. The blue lines show the location of the gathers.

Downloaded 01/23/16 to 138.67.128.33. Redistribution subject to SEG license or copyright; see Terms of Use at http://library.seg.org/

final images for both inversions. The inversion using the backscattering shows improvement in the flatness of the second and third layers because it promotes better focusing in the lower part of the model. Without backscattering, the focusing measured in the second layer is only sensitive to the velocity above this layer, whereas with backscattering, we can pick up focusing information from the deepest layers. Adding the sharp boundary is equivalent to putting more weight on the focusing error of the deepest reflector.

As mentioned in the previous section, tomography with backscattering requires iterative update of the velocity model and the sharp boundary. For this particular inversion problem, we iteratively update the boundary position from depth to time using the velocity $V^{it}(\mathbf{x})$ and stretching back to depth using the velocity $V^{it+1}(\mathbf{x})$, where the superscript relates to the iteration number. This scheme implicitly assumes that the vertical traveltime is preserved. For stretching to time, we use

$$t_i = t_{i-1} + \frac{z_i^{it} - z_{i-1}^{it}}{V^{it}(z_i)}, \tag{21}$$

with $t_0 = 0$, and for stretching back to depth, we use

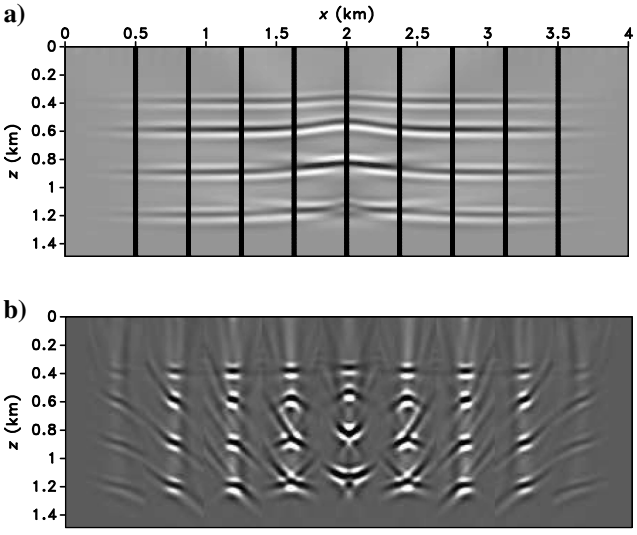


Figure 9. (a) Conventional image from the starting model in Figure 6a and (b) and its space-lag gathers. Note how the backscattering spreads the defocusing of the events in the conventional image (top). Compare with optimized image in Figure 11b.

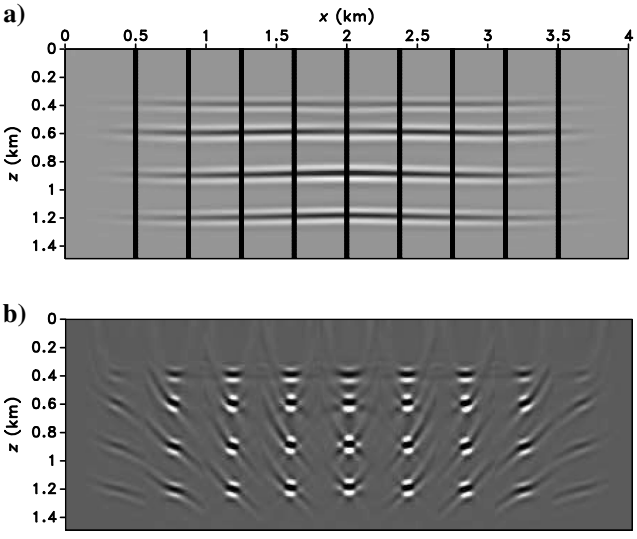


Figure 10. (a) Conventional image from inverted model without the sharp boundary and (b) its space-lag gathers.

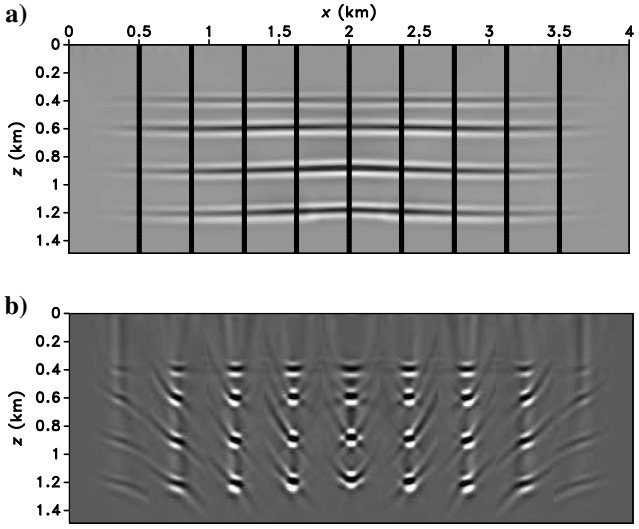


Figure 11. (a) Conventional image from inverted model with the sharp boundary and (b) its space-lag gathers.

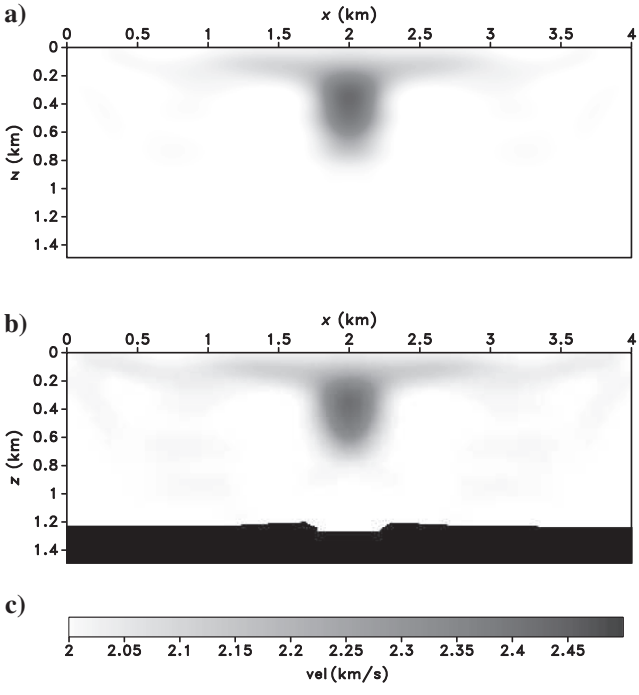


Figure 12. (a) Final inverted velocity models without the sharp boundary, (b) with the sharp boundary, and (c) the corresponding color bar.

$$z_i^{it+1} = z_{i-1}^{it+1} + V^{it+1}(z_i)(t_i - t_{i-1}). \quad (22)$$

This vertical stretching assumes that the traveltime is affected only by the velocity above the sharp boundary, so it would be naive to use it under strong lateral velocity variations as explained in Cameron et al. (2008). An effective alternative could be a zero-offset migration/demigration scheme for updating the sharp boundary. Nevertheless, this approach works for this example and it helps us illustrate the strengths of the methodology. To help correct accumulated prediction errors during the iterative process, one could repick the boundary after some iterations or allow an alternative automatic process to move a known interface based on an updated image.

Finally, Figure 12a and 12b shows the inverted models without the sharp boundary and with the sharp boundary strategy, respectively. We can observe that the inverted model with the sharp boundary has fewer side lobes around the recovered anomaly and higher velocity at the anomaly. Despite the fact that the recovered anomaly for the sharp boundary better focuses the events, the geometry of the sharp boundary is not flat. The inaccurate boundary prediction is due to the lateral homogeneous assumption for predicting the sharp boundary.

Downloaded 01/23/16 to 138.67.128.33. Redistribution subject to SEG license or copyright; see Terms of Use at http://library.seg.org/

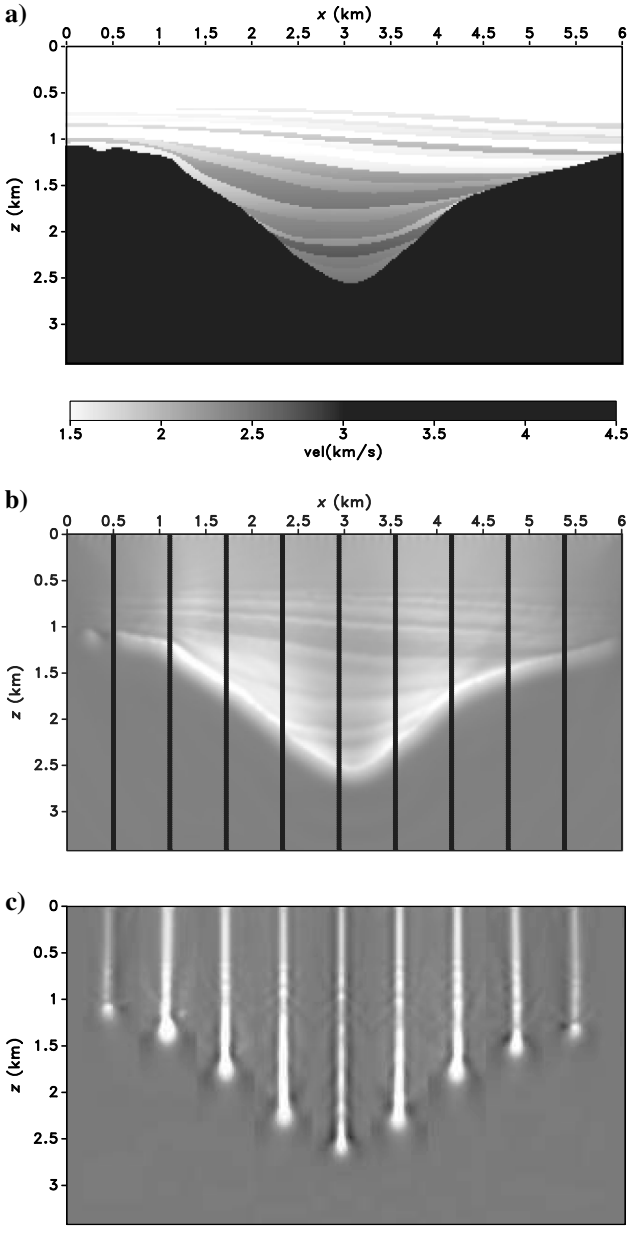


Figure 13. (a) True velocity model, (b) migrated data using the true model, and (c) space lag.

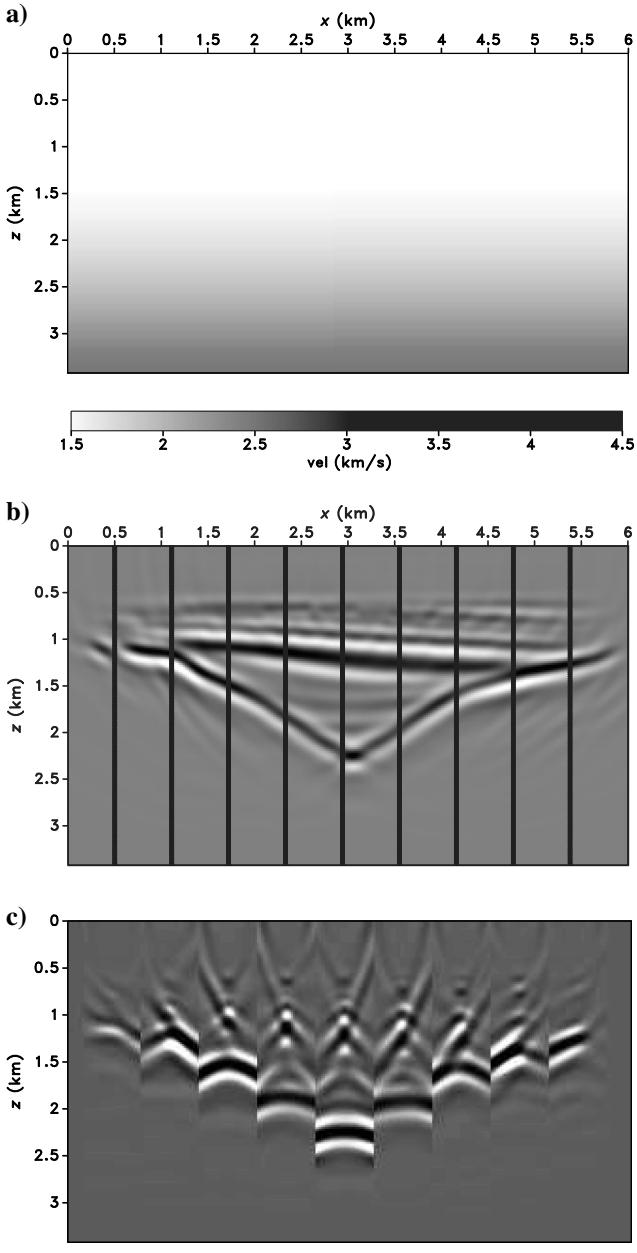


Figure 14. (a) Starting velocity model, (b) conventional image from starting model, and (c) its space-lag gathers.

Downloaded 01/23/16 to 138.67.128.33. Redistribution subject to SEG license or copyright; see Terms of Use at http://library.seg.org/

Complex model based on the Sigsbee2B velocity

Here, we illustrate the use of the backscattering and reflected events on a small portion of the Sigsbee2B model (Paffenholz et al., 2002). We focus on the small basin formed by the salt intrusion (Figure 13a) due to its structural complexity and because it generates considerable backscattering energy. We simulate data for 61 shots evenly distributed on the surface, with a fixed receiver array at the surface. Figure 13b shows the migrated data using the correct velocity model, and Figure 13c shows the corresponding space-lag gathers. The λ_x axis goes from -0.4 to $+0.4$ km for all cases in this section.

Similar to our work with the previous example, we perform two inversion tests: one with the conventional strategy and the other with the new method. We test the method using a slow sediment velocity with an error increasing with depth, as shown in Figure 14a. Figure 14b depicts the RTM image for this model, and Figure 15c shows the corresponding space-lag gathers. We interpret a salt boundary from the RTM image with slow sediment velocity, and we add the salt layer to the model as shown in Figure 15a. Note how the incorrect velocity model, along with the inaccurate boundary, produces strong artifacts in the image. These artifacts are produced because the $R^{ff}(\mathbf{x})$ and $R^{bb}(\mathbf{x})$ components of the image do not map to the same position for incorrect velocity. Figure 15c and

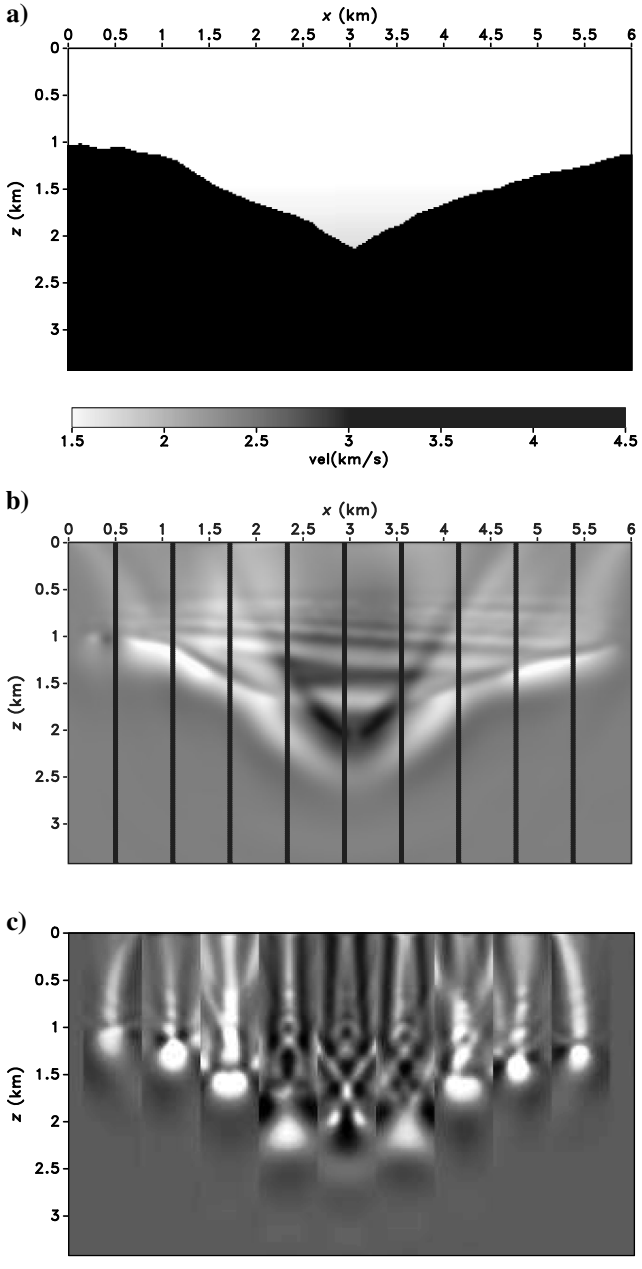


Figure 15. (a) Starting velocity model with sharp boundary, (b) corresponding migrated image, and (c) its space-lag gathers. Note the strong backscattering and its spread from $\lambda_x = 0$.

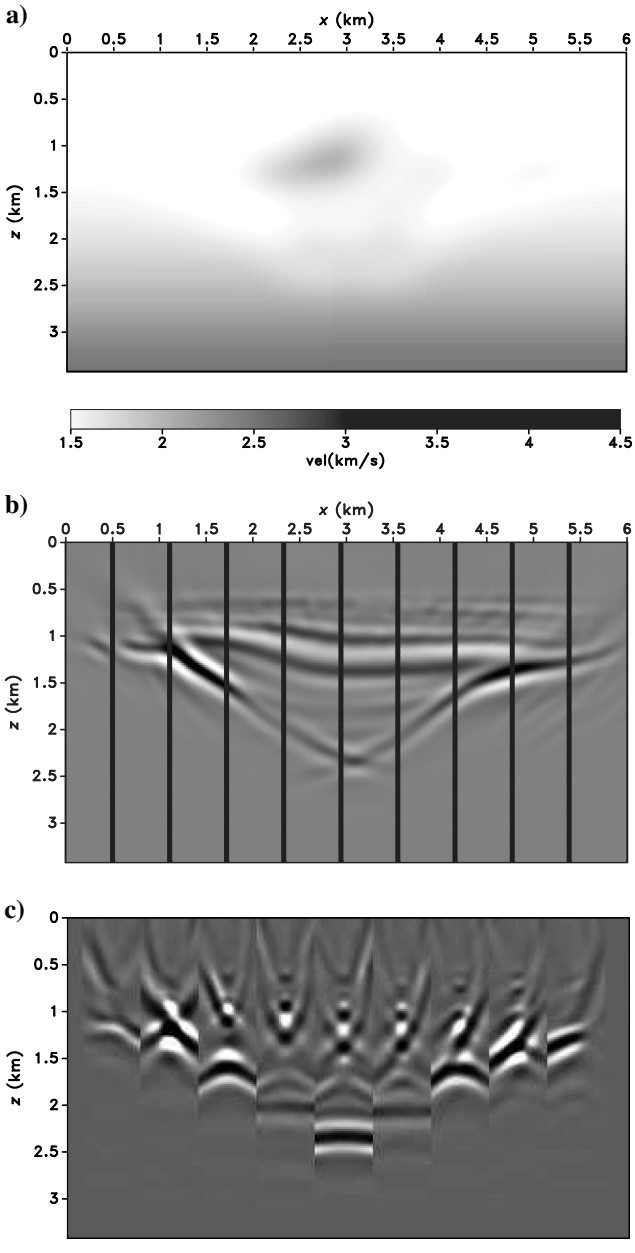


Figure 16. (a) Final inverted model for the conventional approach, (b) final migrated image, and (c) the corresponding space-lag gathers.

Downloaded 01/23/16 to 138.67.128.33. Redistribution subject to SEG license or copyright; see Terms of Use at http://library.seg.org/

15c shows the RTM image and the respective space-lag gathers for the starting velocity with the sharp boundary. Note how the backscattering in Figure 15c spreads away from zero lag. It is worth noticing how the backscattering in the RTM image (Figure 15b) varies throughout the section and produces two events originating in the deepest part of the basin.

The inversion without backscattering has difficulties updating the model inside the basin, and it produces an anomaly near the water bottom as depicted in Figure 16a. This velocity produces incorrect reflector depths, as shown by the image in Figure 16b; however, the corresponding space-lag gathers, Figure 16c, show good focusing.

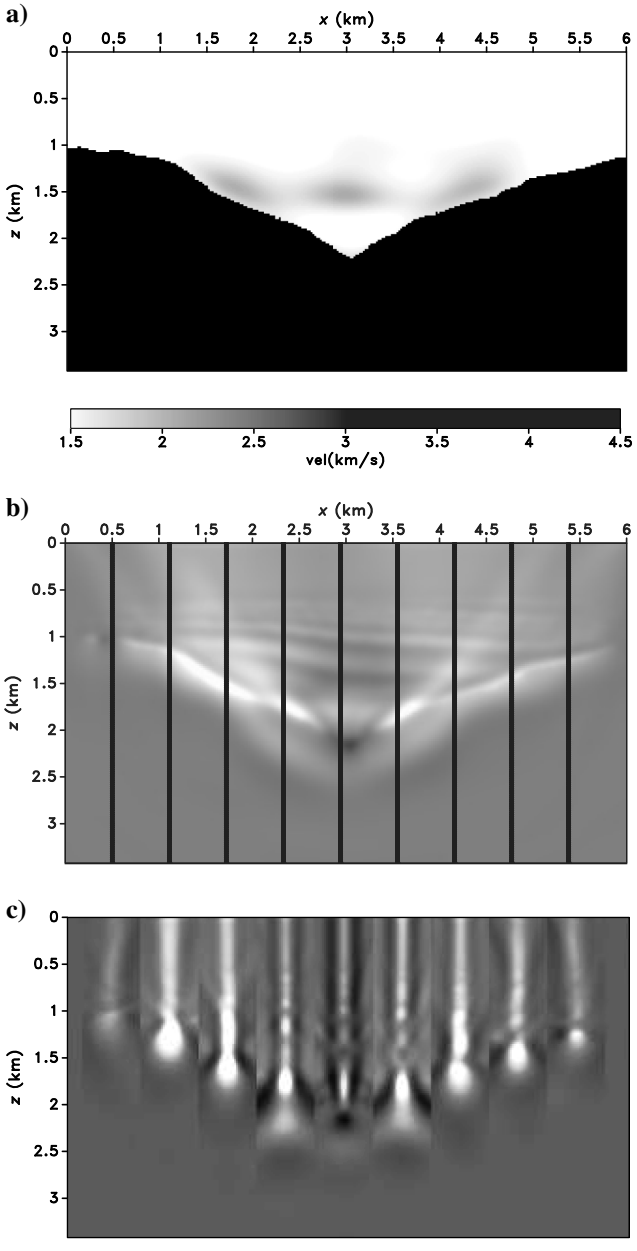


Figure 17. (a) Final inverted model with sharp boundary, (b) final migration image, and (c) its corresponding space-lag gathers. Note how the backscattering energy has been optimized and placed around $\lambda_x = 0$.

Figure 17a shows the final inverted model using the new method; note how the velocity inside the basin is better retrieved than in the conventional approach. Figure 17b and 17c shows the final RTM image and the corresponding gathers, respectively. Note how the inverted model correctly focuses all the energy to zero lag. Also, the final gathers have simpler characteristics (without crossing events) compared with those of Figure 15c. The backscattering event is consistent throughout the section. This consistency of the backscattering can also be seen in the final RTM image, Figure 17c. For updating the boundary, we use the same strategy as in the previous example. Despite not being consistent with the lateral homogeneous assumption, the top of salt (TOS) event moves down in the right direction as the velocity in the sediments increases.

CONCLUSIONS

We have demonstrated that RTM backscattering contains kinematic and focusing information that can be used for wavefield tomography. To include the backscattering in the tomography, we need sharp boundaries in the model. During the tomographic iterations, the velocity model and the sharp boundaries need to be updated. The sharp boundaries generate waves traveling in all directions for state and adjoint state wavefields. Therefore, the gradient contains smooth and sharp components produced by the correlation of waves traveling in similar and opposite directions, respectively. We use a directional filter based on Poynting vectors to isolate the gradient components corresponding to the correlation of waves traveling in the same direction. Our numerical experiments indicate that the model is better retrieved when we include the boundary in the inversion due to the fact that backscattering spreads information observed at the sharp boundary everywhere in the medium, increasing the weight of the deepest events during the tomographic update. The setup proposed in this paper leads to increased focusing of reflected energy above the boundary while at the same time maximizing the backscattered energy.

ACKNOWLEDGMENTS

We acknowledge the support of the sponsors of the Center for Wave Phenomena at the Colorado School of Mines. The numeric examples in this paper use the Madagascar open-source software package, freely available from http://www.ahay.org. We would also like to acknowledge the stimulating discussions with N. Patrikeeva and T. Yang about the Poynting vector and wavefield tomography, respectively. We would like to thank the constructive and useful comments from associate editor J. Schleicher, Y. Zhang, and two anonymous reviewers.

APPENDIX A

ADJOINT-STATE FORMULATION

In this section, we show the derivation for the adjoint sources for time-lag-gather and space-lag-gather tomography. This derivation is similar to that of Weibull and Arntsen (2013), who also use a two-way operator and Shen (2004), who uses a one-way extrapolation operator. We follow the approach explained in Plessix (2006).

Let us first remember some notation from the body of the paper. The OF depends on the model $m(\mathbf{x}) = v(\mathbf{x})$, the source wavefield $u_s(\mathbf{x}, t)$, and the receiver wavefield $u_r(\mathbf{x}, t)$. The dependency of the

Downloaded 01/23/16 to 138.67.128.33. Redistribution subject to SEG license or copyright; see Terms of Use at http://library.seg.org/

wavefields is embedded inside the extended image, defined in equation 7. From here on, we omit the dependency of the variables with space ($\mathbf{x}$) and time (t) to eliminate clutter in the derivation.

Space-lag gathers

The OF

$$J(m) = \frac{1}{2}\|P(\boldsymbol{\lambda})R(\mathbf{x},\boldsymbol{\lambda})\|^2, \tag{A-1}$$

depends on the wavefields, so we can think about it as the functional

$$h(u_s, u_r, m) = J(m). \tag{A-2}$$

We then define the Lagrangian with equality constraints on the solution to the wave equation:

$$\mathcal{L}(u_s, u_r, a_s, a_r, m) = h(u_s, u_r, m) - \langle a_s, F_s(u_s, m)\rangle - \langle a_r, F_r(u_r, m)\rangle, \tag{A-3}$$

with $F_s = [(1/v(\mathbf{x})^2)(\partial^2 u_s/\partial t^2)] - \nabla^2 u_s - f_s$ and $F_r = [(1/v(\mathbf{x})^2)(\partial^2 u_r/\partial t^2)] - \nabla^2 u_r - d$. Note that F_s solves the wave-equation forward in time and F_r does it in backward mode. The wavefields a_s and a_r are the adjoint source and receiver wavefields, respectively. These wavefields do not depend on the model m.

Because u_s and u_r satisfy the wave equation, then $F_s = 0$ and $F_r = 0$, which implies

$$\mathcal{L}(u_s, u_r, a_s, a_r, m) = h(u_s, u_r, m) = J(m), \tag{A-4}$$

for any a_s or a_r. Hence, the following condition always holds:

$$\frac{\partial \mathcal{L}(u_s, u_r, a_s, a_r, m)}{\partial m} = \frac{\partial h(u_s, u_r, m)}{\partial m} = \frac{\partial J}{\partial m}. \tag{A-5}$$

This implies that computing $\nabla_m J = \partial J/\partial m$ is equivalent to the gradient of the augmented functional $\partial\mathcal{L}/\partial m$. We can compute of the derivatives of the augmented functional with implicit differentiation as follows

$$\delta\mathcal{L} = \frac{\partial \mathcal{L}}{\partial u_s}\partial u_s + \frac{\partial \mathcal{L}}{\partial u_r}\partial u_r + \frac{\partial \mathcal{L}}{\partial m}\partial m. \tag{A-6}$$

We want to collect terms of the above expression at the stationary point by Plessix (2006). Hence, we must satisfy

$$\frac{\partial \mathcal{L}}{\partial u_s}\partial u_s = 0, \tag{A-7}$$

and

$$\frac{\partial \mathcal{L}}{\partial u_r}\partial u_r = 0, \tag{A-8}$$

which lead into the so-called adjoint-state equations.

From equation A-7, we obtain

$$\frac{1}{v(\mathbf{x})^2}\frac{\partial^2 a_s(\mathbf{x},t)}{\partial t^2} - \nabla^2 a_s(\mathbf{x},t) = \sum_{\boldsymbol{\lambda}} \boldsymbol{\lambda}^2 R(\mathbf{x}-\boldsymbol{\lambda},\boldsymbol{\lambda}) u_s(\mathbf{x}-2\boldsymbol{\lambda},t), \tag{A-9}$$

which is solved backward in time, and

$$\frac{1}{v(\mathbf{x})^2}\frac{\partial^2 a_r(\mathbf{x},t)}{\partial t^2} - \nabla^2 a_r(\mathbf{x},t) = \sum_{\boldsymbol{\lambda}} \boldsymbol{\lambda}^2 R(\mathbf{x}-\boldsymbol{\lambda},\boldsymbol{\lambda}) u_r(\mathbf{x}-2\boldsymbol{\lambda},t), \tag{A-10}$$

for the receiver wavefield side, which is solved forward in time. The right side in equations A-14 and A-10 corresponds to the adjoint source formulas shown in equations 19 and 20, respectively.

Finally, the gradient is computed from the last condition in equation A-6 from which we obtain

$$\nabla_m J = \frac{-2}{v^3(\mathbf{x})}\sum_e\sum_t \frac{\partial^2 u_s}{\partial t^2}(e,\mathbf{x},t) a_s(e,\mathbf{x},t) + \frac{\partial^2 u_r}{\partial t^2}(e,\mathbf{x},t) a_r(e,\mathbf{x},t). \tag{A-11}$$

Time-lag gathers

The formulation for time-lag gathers is very similar to the one of space-lag gathers. We start by defining the OF

$$J(m) = \frac{1}{2}\|P(\tau)R(\mathbf{x},\tau)\|^2, \tag{A-12}$$

and then we follow steps A-3–A-8. Thus, we reach the adjoint-state equations,

$$\frac{1}{v(\mathbf{x})^2}\frac{\partial^2 a_s(\mathbf{x},t)}{\partial t^2} - \nabla^2 a_s(\mathbf{x},t) = \sum_{\boldsymbol{\lambda}} \tau^2 R(\mathbf{x},\tau) u_r(\mathbf{x},t-2\tau), \tag{A-13}$$

which is solved backward in time, and

$$\frac{1}{v(\mathbf{x})^2}\frac{\partial^2 a_r(\mathbf{x},t)}{\partial t^2} - \nabla^2 a_r(\mathbf{x},t) = \sum_{\boldsymbol{\lambda}} \tau^2 R(\mathbf{x},\tau) u_r(\mathbf{x},t+2\tau), \tag{A-14}$$

which is solved forward in time.

Once we solve for state and adjoint-state variables, we compute the gradient using the same expression as equation A-11.

REFERENCES

Baysal, E., D. D. Kosloff, and J. W. C. Sherwood, 1983, Reverse time migration: Geophysics, **48**, 1514–1524, doi: 10.1190/1.1441434.

Cameron, M., S. Fomel, and J. Sethian, 2008, Time-to-depth conversion and seismic velocity estimation using time-migration velocity: Geophysics, **73**, no. 5, VE205–VE210, doi: 10.1190/1.2967501.

Claerbout, J. F., 1971, Toward a unified theory of reflector mapping: Geophysics, **36**, 467–481, doi: 10.1190/1.1440185.
Clément, F., G. Chavent, and S. Gmez, 2001, Migration-based traveltime waveform inversion of 2-D simple structures: A synthetic example: Geophysics, **66**, 845–860, doi: 10.1190/1.1444974.
Díaz, E., and P. Sava, 2012, Understanding the reverse time migration backscattering: Noise or signal?: 82nd Annual International Meeting, SEG, Expanded Abstracts, doi: 10.1190/segam2012-1203.1.
Etgen, J., S. Gray, and Y. Zhang, 2009, An overview of depth imaging in exploration geophysics: Geophysics, **74**, no. 6, WCA5–WCA17, doi: 10.1190/1.3223188.
Fei, T. W., Y. Luo, and G. T. Schuster, 2010, De-blending reverse-time migration: 80th Annual International Meeting, SEG, Expanded Abstracts, 3130–3134.
Fletcher, R. F., P. Fowler, P. Kitchenside, and U. Albertin, 2005, Suppressing artifacts in prestack reverse time migration: 75th Annual International Meeting, SEG, Expanded Abstracts, 2049–2051.
Fliedner, M., and D. Bevc, 2008, Automated velocity model building with wavepath tomography: Geophysics, **73**, no. 5, VE195–VE204, doi: 10.1190/1.2957892.
Gray, S., J. Etgen, J. Dellinger, and D. Whitmore, 2001, Seismic migration problems and solutions: Geophysics, **66**, 1622–1640, doi: 10.1190/1.1487107.
Guitton, A., B. Kaelin, and B. Biondi, 2007, Least-squares attenuation of reverse-time-migration artifacts: Geophysics, **72**, no. 1, S19–S23, doi: 10.1190/1.2399367.
Kaelin, B., and C. Carvajal, 2011, Eliminating imaging artifacts in RTM using pre-stack gathers: 81st Annual International Meeting, SEG, Expanded Abstracts, 3125–3129.
Liu, F., G. Zhang, S. A. Morton, and J. P. Leveille, 2011, An effective imaging condition for reverse time migration using wavefield decomposition: Geophysics, **76**, no. 1, S29–S39, doi: 10.1190/1.3533914.
Ma, Y., and D. Hale, 2013, Wave-equation reflection traveltime inversion with dynamic warping and full-waveform inversion: Geophysics, **78**, no. 6, R223–R233, doi: 10.1190/geo2013-0004.1.
McMechan, G. A., 1983, Migration by extrapolation of time-dependent boundary values: Geophysical Prospecting, **31**, 413–420, doi: 10.1111/j.1365-2478.1983.tb01060.x.
Paffenholz, J., B. McLain, J. Zaske, and P. Keliher, 2002, Subsalt multiple attenuation and imaging: Observations from the Sigsbee2B synthetic dataset: 72nd Annual International Meeting, SEG, Expanded Abstracts, 2122–2125.
Plessix, R.-E., 2006, A review of the adjoint-state method for computing the gradient of a functional with geophysical applications: Geophysical Journal International, **167**, 495–503, doi: 10.1111/j.1365-246X.2006.02978.x.
Pratt, R. G., 1999, Seismic waveform inversion in the frequency domain, Part I: Theory and verification in a physical scale model: Geophysics, **64**, 888–901, doi: 10.1190/1.1444597.
Rickett, J. E., and P. C. Sava, 2002, Offset and angle-domain common image-point gathers for shot-profile migration: Geophysics, **67**, 883–889, doi: 10.1190/1.1484531.
Sava, P., and B. Biondi, 2004, Wave-equation migration velocity analysis — I: Theory: Geophysical Prospecting, **52**, 593–606, doi: 10.1111/j.1365-2478.2004.00447.x.
Sava, P. C., and S. Fomel, 2003, Angle-domain common-image gathers by wavefield continuation methods: Geophysics, **68**, 1065–1074, doi: 10.1190/1.1581078.
Sava, P., and S. Fomel, 2006, Time-shift imaging condition in seismic migration: Geophysics, **71**, no. 6, S209–S217, doi: 10.1190/1.2338824.
Sava, P., and I. Vasconcelos, 2011, Extended imaging conditions for wave-equation migration: Geophysical Prospecting, **59**, 35–55, doi: 10.1111/j.1365-2478.2010.00888.x.
Sava, P., and I. Vlad, 2011, Wide-azimuth angle gathers for wave-equation migration: Geophysics, **76**, no. 3, S131–S141, doi: 10.1190/1.3560519.
Shen, P., 2004, Wave equation migration velocity analysis by differential semblance optimization: Ph.D. thesis, Rice University.
Shen, P., and W. W. Symes, 2008, Automatic velocity analysis via shot profile migration: Geophysics, **73**, no. 5, VE49–VE59, doi: 10.1190/1.2972021.
Shen, P., W. W. Symes, and C. C. Stolk, 2003, Differential semblance velocity analysis by wave equation migration: 73rd Annual International Meeting, SEG, Expanded Abstracts, 2132–2135.
Sirgue, L., and R. Pratt, 2004, Efficient waveform inversion and imaging: A strategy for selecting temporal frequencies: Geophysics, **69**, 231–248, doi: 10.1190/1.1649391.
Stork, C., 1992, Reflection tomography in the postmigrated domain: Geophysics, **57**, 680–692, doi: 10.1190/1.1443282.
Symes, W. W., 2007, Reverse time migration with optimal checkpointing: Geophysics, **72**, no. 5, SM213–SM221, doi: 10.1190/1.2742686.
Symes, W., and J. Carazzone, 1991, Velocity inversion by differential semblance optimization: Geophysics, **56**, 654–663, doi: 10.1190/1.1443082.
Tarantola, A., 1984, Inversion of seismic reflection data in the acoustic approximation: Geophysics, **49**, 1259–1266, doi: 10.1190/1.1441754.
Weibull, W., and B. Arntsen, 2013, Automatic velocity analysis with reverse-time migration: Geophysics, **78**, no. 4, S179–S192, doi: 10.1190/geo2012-0064.1.
Whitmore, N. D., 1983, Iterative depth migration by backward time propagation: 53rd Annual International Meeting, SEG, Expanded Abstracts, 382–385.
Woodward, M., 1992, Wave-equation tomography: Geophysics, **57**, 15–26, doi: 10.1190/1.1443179.
Xu, S., D. Wang, F. Chen, Y. Zhang, and G. Lambare, 2012, Full waveform inversion for reflected seismic data: 74th Annual International Conference and Exhibition, EAGE, Extended Abstracts, W024.
Yang, T., and P. Sava, 2010, Moveout analysis of wave-equation extended images: Geophysics, **75**, no. 4, S151–S161, doi: 10.1190/1.3460296.
Yang, T., and P. Sava, 2011a, Image-domain waveform tomography with two-way wave-equation: 81st Annual International Meeting, SEG, Expanded Abstracts, 2591–2596.
Yang, T., and P. Sava, 2011b, Wave-equation migration velocity analysis with time-shift imaging: Geophysical Prospecting, **59**, 635–650, doi: 10.1111/j.1365-2478.2011.00954.x.
Yang, T., J. Shragge, and P. Sava, 2013, Illumination compensation for image-domain wavefield tomography: Geophysics, **78**, no. 5, U65–U76, doi: 10.1190/geo2012-0278.1.
Yoon, K., K. J. Marfurt, and W. Starr, 2004, Challenges in reverse time migration: 74th Annual International Meeting, SEG, Expanded Abstracts, 1057–1060.
Youn, O. K., and H. Zhou, 2001, Depth imaging with multiples: Geophysics, **66**, 246–255, doi: 10.1190/1.1444901.
Zhang, Y., and J. Sun, 2009, Practical issues in reverse time migration: True amplitude gathers, noise removal and harmonic source encoding: First Break, **27**, 53–59, doi: 10.3997/1365-2397.2009002.

Downloaded 01/23/16 to 138.67.128.33. Redistribution subject to SEG license or copyright; see Terms of Use at http://library.seg.org/